Research Article

A two-dimensional finite element model of cyclic adenosine monophosphate (cAMP) intracellular signaling

N. Stone[1] · S. Shettlesworth[1] · T. C. Rich[2] · S. J. Leavesley[3] · A. -V. Phan[1]

Abstract

In this work, we present a two-dimensional finite element analysis (FEA) model that describes fundamental intracellular signals of cyclic adenosine monophosphate (cAMP) in a general fashion. The model was subsequently solved numerically and the results were displayed in forms of time-course plots of cAMP concentration at a cellular location or color-filled contour maps of cAMP signal distribution within the cell at specific time points. Basic intracellular cAMP signaling was described in this model so it can be numerically validated by verifying its numerical results against available analytical solutions and against results obtained from other numerical techniques reported in the literature. This is the first important step before the model can be expanded in future work. Model simulations demonstrate that under certain conditions, sustained cAMP concentrations can be formed within endothelial cells (ECs), similar to those observed in rat pulmonary microvascular ECs. Spatial and temporal cAMP dynamic simulations indicated that the proposed FEA model is an effective tool for the study of the kinetics and spatial spread of second messenger signaling and can be expanded to simulate second messenger signals in the pulmonary vasculature.

1 Introduction

Intracellular signals are responsible for a multitude of cellular functions, and cyclic adenosine monophosphate (cAMP) is one of these signals. cAMP is a second messenger that regulates a plethora of cellular functions, including cell metabolism, cell proliferation, and cell movement, e.g., [1, 2]. cAMP is produced in response to stimulation of G_s coupled receptors, which trigger activation of G_s and subsequent stimulation of adenylyl cyclase (AC) activity. cAMP levels then increase which leads to activation of downstream effectors, including protein kinase A (PKA), exchange protein activated by cAMP (Epac), and ion channels. Phosphodiesterases (PDEs) are a family of enzymes that degrade cAMP. Pharmaceutical agents that regulate cAMP levels, including G_s coupled receptor agonists and antagonists, and phosphodiesterase inhibitors, have been used to treat diseases such as diabetes, asthma, and cardiac failure, e.g., [3, 4].

In the last decade it has become apparent that the subcellular localization of cAMP is a critical component of signaling specificity. Specifically, cAMP synthesized at the plasma membrane increases the barrier integrity of endothelial cells (ECs), whereas cAMP produced by soluble cyclase (sAC) triggers a reduction in endothelial barrier integrity. While we understand a great deal about the cAMP pathway, we still do not understand well the roles of cAMP signals and how information is

encoded within these signals, having only a rudimentary understanding of the spatial distributions of cAMP signals inside a cell [5–7]. A range of numerical approaches have been employed to model intracellular signaling of second messengers. Finite volume method (FVM) was used to develop a system called "Virtual Cell" [8] with the goal of modeling cellular structure and function. In [9], deterministic mathematical models of the cAMP pathway were created, however spatial spreads of cAMP signals were not considered in these models. Additionally, a large scale stochastic simulation was used as a way to predict cAMP signaling in a variety of cellular environments [10], and a fourth-order Runge–Kutta numerical technique was used to model cAMP signals near the plasma membrane of HEK-293 cells [11]. Recently, our group used the "Virtual Cell" environment with the goal to explore cellular mechanisms contributing to cAMP compartmentalization in pulmonary microvascular ECs [12]. One of the striking outcomes of this study, the results of which have been validated both experimentally and in subsequent computational studies, is that the rate of cAMP diffusion within cells is markedly slower than would be expected if cytosol had similar properties as salt water [6, 13–16].

The objective of this work is to use finite element method (FEM) to simulate basic mechanisms of cAMP intracellular signaling in a general fashion. FEM is a popularly used engineering technique. It is widely recognized as a powerful numerical method for solving challenging engineering and mathematical problems. The method offers much flexibility in handling problems involving complex geometries such as those of ECs. An important mechanism in cAMP intracellular signaling is cAMP diffusion, and FEM has been known as a very effective and accurate technique for numerical implementation of diffusion equations. Another advantage of FEM is its ability to easily handle mixed formulations arising from multiphysics simulations. This FEM feature is particularly important to modeling of the cAMP signaling pathway as new cell biological mechanisms will likely be detected in the future, and that could require the use of mixed formulations.

To develop our proposed FEA cAMP signaling model, a general governing equation, in the form of a partial differential equation, of cAMP synthesis, diffusion, and degradation was first introduced. FEM was then employed to discretize this governing equation, using three-node triangular elements, into systems of ordinary differential equations. By solving these systems of equations using the time integration method, dynamic simulations in forms of time-course plots of cAMP concentration at different cellular locations or color-filled maps of cAMP distribution within the cell at different time instants can be obtained.

Note that some previous studies of our group also used FEA for modeling cAMP intracellular signaling in a two-dimensional (2-D) [17] and 3-D geometry [18] of a single cell. However, the FEA models developed in those works were based on a linear approximation of the Michaelis–Menten kinetics of PDE enzymes about the initial value of cAMP concentration and thereby, the models are accurate only for low levels of cAMP concentration. Conversely, the FEA model developed in this work employed a quasi-linearization of the Michaelis–Menten equation. The technique is based upon a linear approximation about the exact level of cAMP concentration at any given time. Although the quasi-linearization requires the use of an iterative process, it results in an accurate evaluation of PDE reactions at any levels of cAMP concentration. Additional capabilities were also included in the intracellular cAMP signaling FEA model developed in this work. The new model can simulate a variety of AC and PDE activities anywhere within the cell, including those in the plasmalemmal and perinuclear regions, as well as the time instants when these activities are initiated.

The proposed FEA model was based on fundamental mechanisms of cAMP intracellular signaling so it can be validated using some verifications of its results against available analytical solutions and against results obtained from the "Virtual Cell" software platform. The validation presented in this work is very important for future work where other components of cAMP signaling such as activities of different PDE types can be added to the model.

2 Governing equation

For two-dimensional (2-D) modeling, the equation governing the synthesis, diffusion and degradation of cAMP within cells can be generally described as (see [19, 20])

$$\frac{\partial C}{\partial t} = \begin{cases} D\nabla^2 C & \text{if } t < t_s \\ D\nabla^2 C + E_{AC}(x, y) & \text{if } t_s \leq t < t_d \\ D\nabla^2 C + E_{AC}(x, y) - M(C) & \text{if } t \geq t_d \end{cases} \quad (1)$$

where $C = C(t, x, y)$ is the concentration of cAMP at time t and location defined by the coordinates x and y, E_{AC} is the cAMP synthesis function, D is the effective diffusion coefficient, $M(C)$ is the cAMP degradation function based on the Michaelis–Menten kinetics, and t_s and t_d are the time instants when cAMP synthesis (AC activity) and degradation (PDE activity) start occurring, respectively. It is reasonably assumed that PDE activity does not take place earlier than AC activity ($t_s \leq t_d$).

Under the steady-state assumption,

$$M(C) = \frac{V_{max}C}{K_M + C} \tag{2}$$

where V_{max} is the maximum cAMP hydrolysis rate, and K_M is the Michaelis–Menten constant for cAMP binding to PDE.

As $M(C)$ is a nonlinear function in C, an iterative method will need to be employed in the FEA of the model given by Eq. (1). The iterative technique adopted in this work is based on a quasi-linearization of $M(C)$ about $C = C_1$:

$$
\begin{aligned}
M(C) &= M(C_1) + \left.\frac{dM}{dC}\right|_{C=C_1}(C - C_1) \\
&= \frac{V_{max}K_M}{(K_M + C_1)^2}C + \frac{V_{max}C_1^2}{(K_M + C_1)^2}
\end{aligned}
\tag{3}
$$

To accurately evaluate Eq. (2) using its quasi-linearization (3), at a given time and location, the iteration must be carried out until the difference between the predicted C_1 and the solution C resulting from solving the third equation of system (1) satisfies a chosen convergence criterion.

The possible boundary conditions are

- C is specified;
- Normal derivative (concentration flux) is prescribed along a boundary,

$$D\frac{\partial C}{\partial \boldsymbol{n}} = \beta \tag{4}$$

where $\boldsymbol{n}$ is the normal vector to the boundary and β is a constant. For the proposed FEA model, this concentration flux β can be used to simulate AC activities in the plasmalemmal or perinuclear region of a cell.

3 Finite element implementation of the governing equation

To use Galerkin approximation, we first discretize the cellular geometry into a number of elements. For each element, we multiply Eq. (1) by the shape functions N_i ($i = 1, 2, \ldots, n$, where n is the number of nodes of the chosen type of element) selected as weighting functions and then integrate it over the volume V of the element as follows:

$$
\left.
\begin{aligned}
&\int_V \left(\frac{\partial C}{\partial t} - D\nabla^2 C\right)N_i \, dV = 0 && \text{if } t < t_s \\
&\int_V \left(\frac{\partial C}{\partial t} - D\nabla^2 C - E_{AC}(x,y)\right)N_i \, dV = 0 && \text{if } t_s \le t < t_d \\
&\int_V \left(\frac{\partial C}{\partial t} - D\nabla^2 C + aC - b\right)N_i \, dV = 0 && \text{if } t \ge t_d
\end{aligned}
\right\}
\tag{5}
$$

where ∇^2 is the Laplacian, and

$$
\begin{aligned}
a &= \frac{V_{max}K_M}{(K_M + C_1)^2} \\
b &= E_{AC}(x,y) - \frac{V_{max}C_1^2}{(K_M + C_1)^2}
\end{aligned}
\tag{6}
$$

By using Gauss's divergence theorem on the diffusion term and the boundary conditions (see, e.g., [21] for more details), one obtains the following weak form in 2-D:

$$
\left.
\begin{aligned}
&\int_V \left(\frac{\partial C}{\partial t}N_i + D\left(\frac{\partial C}{\partial x}\frac{\partial N_i}{\partial x} + \frac{\partial C}{\partial y}\frac{\partial N_i}{\partial y}\right)\right)dV = 0 && \text{if } t < t_s \\
&\int_V \left(\frac{\partial C}{\partial t}N_i + D\left(\frac{\partial C}{\partial x}\frac{\partial N_i}{\partial x} + \frac{\partial C}{\partial y}\frac{\partial N_i}{\partial y}\right)\right)dV \\
&\quad = \beta\int_{S_n} N_i \, dS + \int_V E_{AC}N_i \, dV && \text{if } t_s \le t < t_d \\
&\int_V \left(\frac{\partial C}{\partial t}N_i + D\left(\frac{\partial C}{\partial x}\frac{\partial N_i}{\partial x} + \frac{\partial C}{\partial y}\frac{\partial N_i}{\partial y}\right) + aC\,N_i\right)dV \\
&\quad = \beta\int_{S_n} N_i \, dS + \int_V b\,N_i \, dV && \text{if } t \ge t_d
\end{aligned}
\right\}
\tag{7}
$$

where S_n is the surface of the element over which its concentration flux is specified.

In this equation, the concentration C of cAMP is interpolated over the element from the nodal values $c_1, c_2, \ldots, c_n$ using the shape functions $N_1, N_2, \ldots, N_n$ as follows:

$$C = [N_1 \, N_2 \cdots N_n]\begin{Bmatrix} c_1 \\ c_2 \\ \vdots \\ c_n \end{Bmatrix} = [N]\{c\} \tag{8}$$

Thus the time derivative of C and its gradients are given by

$$\frac{\partial C}{\partial t} = [N_1 \, N_2 \cdots N_n]\begin{Bmatrix} \dot{c}_1 \\ \dot{c}_2 \\ \vdots \\ \dot{c}_n \end{Bmatrix} = [N]\{\dot{c}\} \tag{9}$$

$$\begin{Bmatrix} \frac{\partial C}{\partial x} \\ \frac{\partial C}{\partial y} \end{Bmatrix} = \begin{bmatrix} \frac{\partial N_1}{\partial x} & \frac{\partial N_2}{\partial x} & \cdots & \frac{\partial N_n}{\partial x} \\ \frac{\partial N_1}{\partial y} & \frac{\partial N_2}{\partial y} & \cdots & \frac{\partial N_n}{\partial y} \end{bmatrix}\begin{Bmatrix} c_1 \\ c_2 \\ \vdots \\ c_n \end{Bmatrix} = [B]\{c\} \tag{10}$$

Substitution of Eqs. (8), (9) and (10) into Eq. (7) results in,

$$
\left.
\begin{aligned}
&[K_1]\{\dot{c}\} + [K_2]\{c\} = \{0\} && \text{if } t < t_s \\
&[K_1]\{\dot{c}\} + [K_2]\{c\} = \{R_1\} + \{R_{2s}\} && \text{if } t_s \le t < t_d \\
&[K_1]\{\dot{c}\} + \big[[K_2] + [K_3]\big]\{c\} = \{R_1\} + \{R_{2b}\} && \text{if } t \ge t_d
\end{aligned}
\right\}
\tag{11}
$$

where

$$[K_1] = \int_V [N]^T[N]\, dV \tag{12}$$

$$[K_2] = \int_V [B]^T[\kappa][B]\, dV \tag{13}$$

$$[\kappa] = D \begin{bmatrix} 1 & 0 \\ 0 & 1 \end{bmatrix} \tag{14}$$

$$= a \int_V [N]^T[N]\, dV \tag{15}$$

$$\{R_1\} = \beta \int_{S_n} [N]^T\, dS \tag{16}$$

$$\{R_{2s}\} = E_{AC} \int_V [N]^T\, dV \quad \text{if } t_s \leq t < t_d \tag{17}$$

$$\{R_{2b}\} = b \int_V [N]^T\, dV \quad \text{if } t \geq t_d \tag{18}$$

In this work, the three-node triangular element of uniform thickness τ (see Fig. 1) was selected for a 2-D numerical implementation of Eq. (11). The shape function matrix of this element is known to be

$$[N] = [1 - \xi - \eta \quad \xi \quad \eta] \tag{19}$$

where ξ and η are the coordinates of the natural coordinate system.

By using these shape functions in Eqs. (12), (13), (15), (16), (17) and (18), one gets

$$[K_1] = \frac{A\tau}{12} \begin{bmatrix} 2 & 1 & 1 \\ 1 & 2 & 1 \\ 1 & 1 & 2 \end{bmatrix} \tag{20}$$

$$[K_2] = A\tau [B]^T[\kappa][B] \tag{21}$$

where

$$[B] = \frac{1}{2A} \begin{bmatrix} y_2 - y_3 & y_3 - y_1 & y_1 - y_2 \\ x_3 - x_2 & x_1 - x_3 & x_2 - x_1 \end{bmatrix} \tag{22}$$

$$[K_3] = a[K_1] \tag{23}$$

$$\{R_1\} = \begin{cases} \beta\tau L_{12}/2[1 \ 1 \ 0]^T & \text{for flux BCs on side 1-2} \\ \beta\tau L_{23}/2[0 \ 1 \ 1]^T & \text{for flux BCs on side 2-3} \\ \beta\tau L_{31}/2[1 \ 0 \ 1]^T & \text{for flux BCs on side 3-1} \end{cases} \tag{24}$$

$$\{R_{2s}\} = \frac{A\tau E_{AC}}{3} \begin{Bmatrix} 1 \\ 1 \\ 1 \end{Bmatrix} \quad \text{if } t_s \leq t < t_d \tag{25}$$

$$\{R_{2b}\} = \frac{A\tau b}{3} \begin{Bmatrix} 1 \\ 1 \\ 1 \end{Bmatrix} \quad \text{if } t \geq t_d \tag{26}$$

In the above equations, (x_i, y_i) are the nodal coordinates of the three-node triangular element under consideration, A is the base area of the element, and L_{ij} is the length of side $i-j$.

At this point, the matrices and vectors in Eqs. (20), (21), (23), (24), (25) and (26) for all elements need to be expanded to the structure/model size before they can be assembled to obtain the global version of the first-order differential Eqs. (11).

By using the time integration method [22], the vector of unknown concentrations $\{c\}_{i+1}$ at time t_{i+1} can be found from $\{c\}_i$ at time t_i as
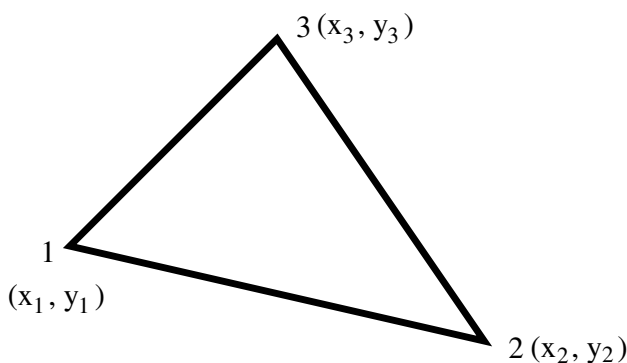

Fig. 1 A three-node triangular element

$$
\left.\begin{array}{ll}
\left[\frac{1}{\Delta t}[K_1] + \gamma[K_2]\right]\{c\}_{i+1} = \left[\frac{1}{\Delta t}[K_1] - (1-\gamma)[K_2]\right]\{c\}_i & \text{if } t < t_s \\[4pt]
\left[\frac{1}{\Delta t}[K_1] + \gamma[K_2]\right]\{c\}_{i+1} = \left[\frac{1}{\Delta t}[K_1] - (1-\gamma)[K_2]\right]\{c\}_i & \\
\qquad + (1-\gamma)\{R_1 + R_{2s}\}_i + \gamma\{R_1 + R_{2s}\}_{i+1} & \text{if } t_s \le t < t_d \\[4pt]
\left[\frac{1}{\Delta t}[K_1] + \gamma[K_2 + K_3]\right]\{c\}_{i+1} = \left[\frac{1}{\Delta t}[K_1] - (1-\gamma)[K_2 + K_3]\right]\{c\}_i & \\
\qquad + (1-\gamma)\{R_1 + R_{2b}\}_i + \gamma\{R_1 + R_{2b}\}_{i+1} & \text{if } t \ge t_d
\end{array}\right\}
\tag{27}
$$

where $\Delta t = t_{i+1} - t_i$ is the time step and system (27) is simply a linear system of algebraic equations of the form

$$[K]\{c\}_{i+1} = \{F\}_{i+1} \tag{28}$$

If some nodal concentrations are prescribed, these boundary conditions must be applied to Eq. (28) to obtain a reduced system of linear equations that contains the vector $\{c_r\}_{i+1}$ of only unknown nodal concentrations at time t_{i+1}.

In this work, Galerkin's implicit method ($\gamma = 2/3$) was chosen to solve the aforementioned reduced system for $\{c_r\}_{i+1}$ as this method is known to be unconditionally stable (no restriction on Δt for obtaining a stable solution) [22]).

For each step time of the time integration method described in Eq. (27), as mentioned before, an iterative process must be utilized for the quasi-linearization of the Michaelis–Menten model. To be specific, the concentration solution $\{c\}_i$ from the previous step time t_i will be used as an initial guess for C_1 employed in evaluating $[K_3]$ and $\{R_2\}$ for calculations at step time t_{i+1} [(see Eqs. (6), (23) and

(26)]. The solution $\{c^*\}_{i+1}$ resulting from using these $[K_3]$ and $\{R_2\}$ is expected to be a better guess for C_1 and this process should be repeated until a chosen convergence criteria is met.

4 Validation of the proposed FEA model

The FEA model presented in the previous section was implemented using custom MATLAB scripts. To validate this model, a number of simulations were run and the FEA results were compared with analytical solutions or those reported in the literature. To run these simulations, we first derived the data for synthesis (E_{AC}), diffusion (D), and degradation (V_{max} and K_M) from those reported in [12] for pulmonary microvascular endothelial cells (PMVECs).

According to [12], $D = 0.3$ to $300\ \mu m^2/s$, $K_M = 2\ \mu M$,

$$E_{AC} = 1200 C_{AC} = (1200\ \text{min}^{-1})(7.06\ \text{nM}) = 0.1412\ \mu M/s \tag{29}$$
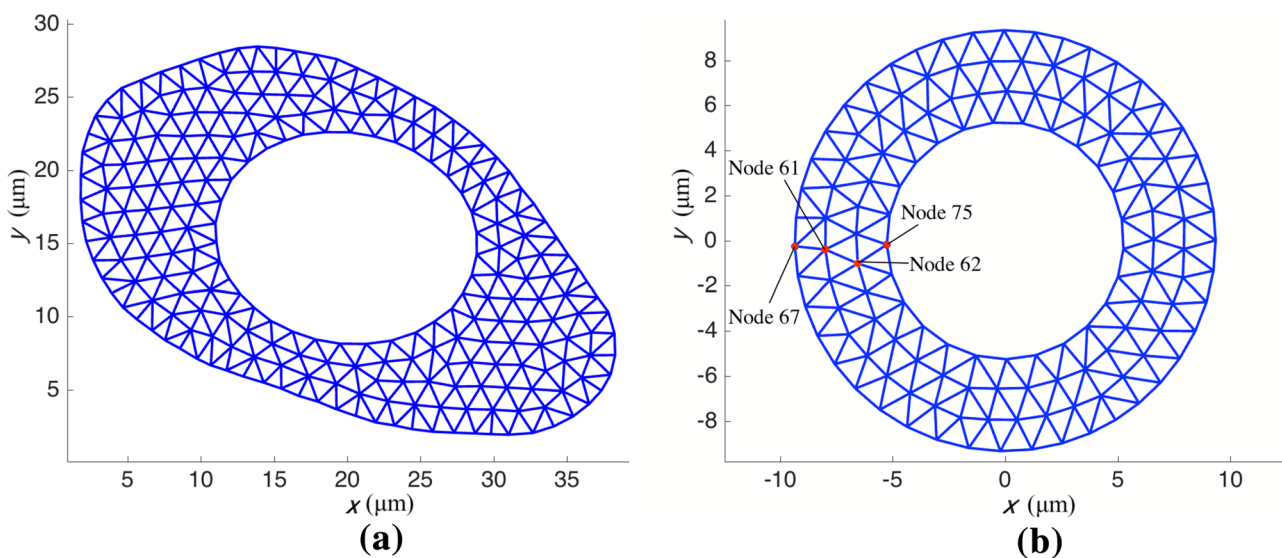
where C_{AC} is the initial AC concentration, and

Fig. 2 FEA meshes for 2-D models of different cellular geometries **a** cultured PMVEC; **b** spherical cell

$K_M = 2\ \mu M$

$$V_{max} = k_{cat}C_{PDE} = (100\ s^{-1})(2.95\ nM) = 0.295\ \mu M/s \qquad (30)$$

where k_{cat} is the cAMP turnover rate and C_{PDE} is the initial PDE enzyme concentration.

Unless otherwise specified, the FEA and analytical results presented in this section were obtained from using the above data and an initial condition of $C_o = 0.05\ \mu M$ (as in [12]). In addition, it was assumed that there is no transport of cAMP signals between the nucleus and the cytoplasm. Note that the proposed FEA model is general which can easily include the transport of cAMP signals as long as data for D, V_{max} and K_M for the nucleus are available. This transport could be considered in a future investigation.

Figure 2a, b depicts FEA meshes for 2-D geometric models of a cultured PMVEC and a spherical cell, respectively. The geometries were based on an individual slice of the respective cells given in [12]. The annulus-shaped geometry was chosen here for the purpose of validating the proposed FEA model as some analytical solutions are available for the diffusion in a hollow cylinder. According to the data in [12], the outer and inner radii of the annulus were determined as $R_o = 9.34\ \mu m$ and $R_i = 5.26\ \mu m$, respectively.

The meshes in Fig. 2a, b were determined from mesh convergence tests and constructed by Distmesh [23] (a MATLAB program that generates and manipulates unstructured 2-D and 3-D meshes and was developed by Per-Olof Persson). The mesh in Fig. 2a consisted of 241 nodes and 375 three-node triangular elements while the mesh in Fig. 2b contained 138 nodes and 208 elements. Some time courses of cAMP signals for the cell model in Fig. 2b were given at four distinct cellular locations represented

by nodes 67 (at the plasma membrane), 75 (at the perinuclear region), and 61 and 62 (in the cytosol).

4.1 Validation against analytical solutions

There is no analytical solution to the governing Eqs. (5). However, in some particular cases, analytical solutions are available for evaluating cAMP concentrations. In this work, we used these particular cases to verify our proposed FEA model.

4.1.1 Verification of the implementation of the Michaelis–Menten equation

If AC and/or PDE activities are uniformly distributed in the cytosolic region, and no-flux boundary conditions are applied along the plasma membrane and the perinuclear region, the time course of cAMP concentration at any cellular location will be the same, resulting in no spatial spread of cAMP. In other words, the result $C(t)$ is independent of cellular geometries, cellular location (x, y) and the effective diffusion coefficient D. This is a case of the so-called compartment models and $C(t)$ is simply the solution of the following ordinary differential equation:

$$\frac{dC}{dt} = E_{AC} - \frac{V_{max}C}{K_M + C} \qquad (31)$$

The analytical solution of this equation is given in "Appendix 1" where $u = E_{AC}$, $v = V_{max}$ and $w = K_M$.
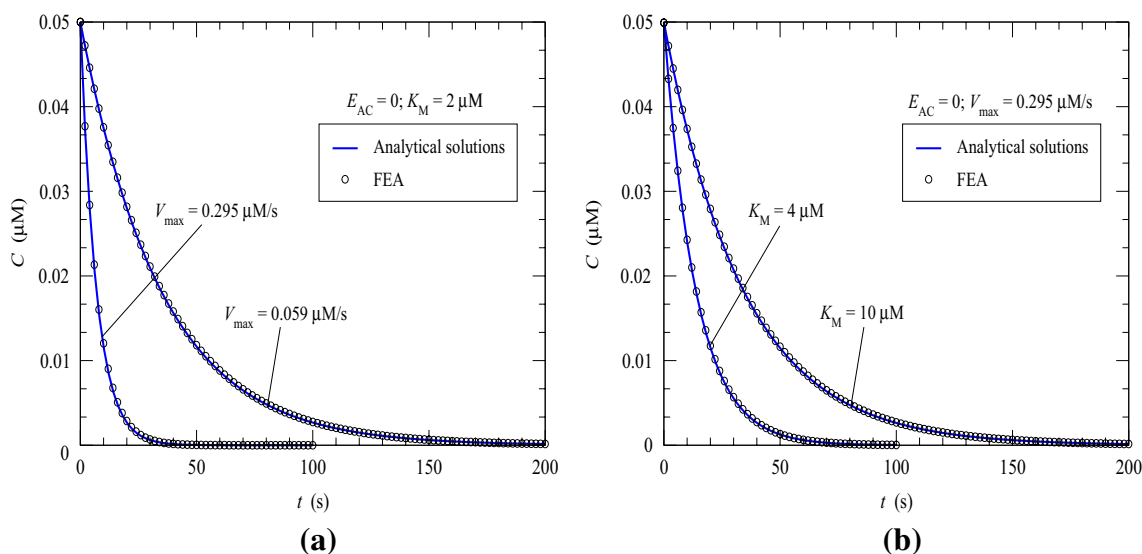

Fig. 3 FEA vs analytical solutions for the time course of cAMP concentration in response to only PDE activity uniformly distributed in the cytosol: **a** Effect of V_{max}; **b** Effect of K_M

To verify the accuracy of implementing the Michaelis–Menten Eq. (2) in this work which used an iterative process with the quasi-linearization (3), a case was considered where AC activity was absent ($E_{AC} = 0$) and PDE activity was uniformly distributed in the cytosol from $t_d = 0$. Both Fig. 3a, b shows excellent agreements between the FEA and analytical solutions (the analytical results were given by Eq. (37) in "Appendix 1") for different scenarios of PDE activities. Regardless of the cellular geometry (Fig. 2a, b) and the diffusion coefficient employed, the FEA results at any nodal location were exactly the same which confirms a case of compartment models as mentioned above. As expected, an increase of V_{max} will result in a quicker drop of cAMP concentration (Fig. 3a), while an increase of K_M will result in a slower drop of cAMP concentration (Fig. 3b).

Of particular interest is a biological significance drawn from the results shown in Fig. 3a, b: the behavior of cAMP signals will be the same for the same ratio of V_{max}/K_M (compare the curve for $V_{max} = 0.059\,\mu M/s$ and $K_M = 2\,\mu M$ in Fig. 3a and the curve for $V_{max} = 0.295\,\mu M/s$ and $K_M = 10\,\mu M$ in Fig. 3b, and note that these two curves have the same ratio $V_{max}/K_M = 0.0295$).

4.1.2 Verification of the implementation of cAMP synthesis

In this section, we first verified the implementation of cAMP synthesis by considering the case where there was no PDE activity ($V_{max} = 0$) while AC activity was uniformly taken place in the cytosol from $t_s = 0$, and no-flux boundary conditions were prescribed at the plasma membrane and in the perinuclear region. As mentioned above, this is a compartment model where the time courses of cAMP concentration are independent of the diffusion coefficient D, cellular geometries and locations, and are given by Eq. (38) in "Appendix 1".

A comparison between the FEA and analytical solutions for three values of $E_{AC} = 0.10, 0.1412$ and $0.16\,\mu M/s$ are shown in Fig. 4a where a very excellent agreement can be seen.

Next, we included a uniform PDE activity ($V_{max} = 0.295\,\mu M/s$, $K_M = 2\,\mu M$) in the cytosol from $t_d = 0$ and again, both the FEA and analytical results (the analytical results were obtained by using Eq. (35) in "Appendix 1") perfectly agree with each other as depicted in Fig. 4b. The figure also reveals that PDE activity resulted in steady-state concentrations of cAMP signals.

4.1.3 Verification of the implementation of cAMP diffusion

Two simulations were carried out to verify the implementation of cAMP diffusion in the proposed FEA model. These simulations employed a diffusion of $D = 30\,\mu m^2/s$ for the annular cell geometry in Fig. 2b which was under the assumption of no AC and PDE activity in the cytosol ($E_{AC} = 0$ and $V_{max} = 0$).

In the first simulation, we applied a concentration $C = 3\,\mu M$ along the cell membrane and $C = 1\,\mu M$ along the periphery of the nucleus. The FEA results for the time courses of cAMP concentration at two cellular locations within the cytosol (nodes 61 and 62, see Fig. 2b) were favorably compared against analytical results as shown in
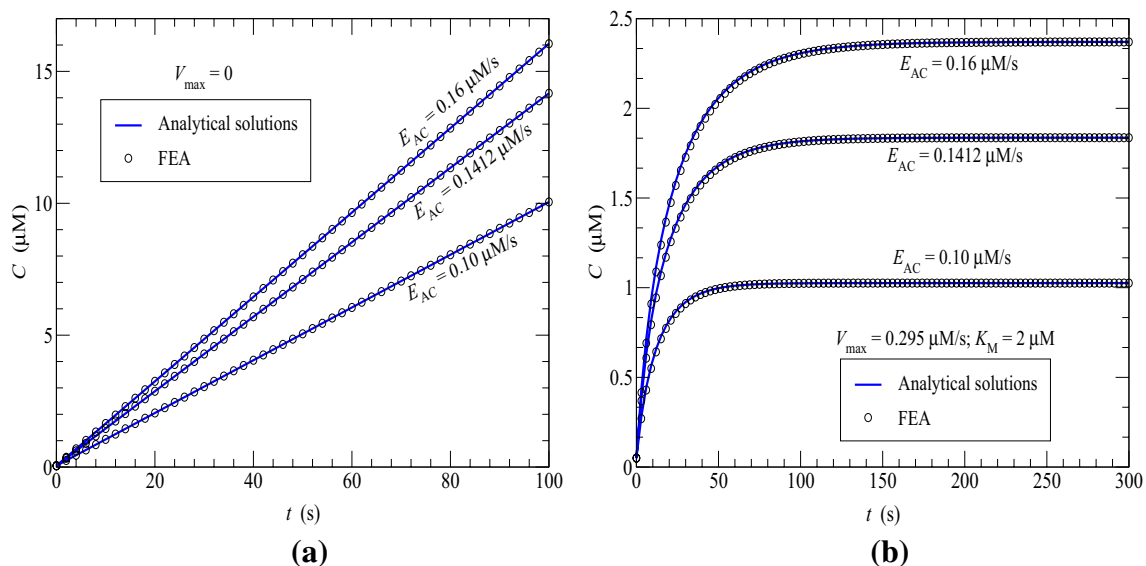

Fig. 4 FEA vs analytical solutions for the time course of cAMP concentration in response to **a** AC activity uniformly distributed in the cytosol; **b** AC and PDE activities uniformly distributed in the cytosol
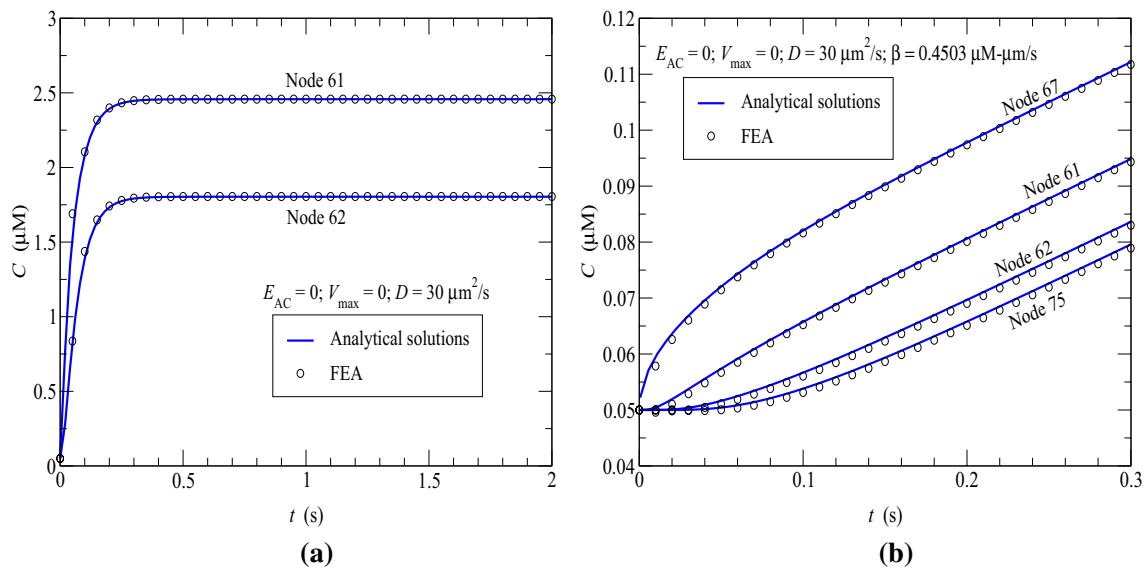
Fig. 5 FEA vs analytical solutions for the time courses of cAMP concentration at different cellular locations in response to diffusion coefficient $D = 30\ \mu m^2/s$ and different boundary conditions:

a $C = 3\ \mu M$ at the plasma membrane and $C = 1\ \mu M$ at the perinuclear region; **b** $\beta = 0.4503\ \mu M \cdot \mu m/s$ at the plasma membrane and $\beta = 0$ at the perinuclear region

Fig. 5a. Note that the analytical solution [24] was derived for the diffusion in a hollow cylinder under concentration boundary conditions and was summarized in Sect. (a) in "Appendix 2".

In the second simulation, we applied a positive flux β along the plasma membrane and a zero flux in the perinuclear region to simulate an AC activity uniformly distributed at the cell membrane.

As in [12], here β was determined under the assumption that the total AC activity produced by AC in the subplasmalemmal region remained the same as AC throughout the cytosolic region. According to this assumption,

$$E_{AC}A_c = \beta S_p \tag{32}$$

where $E_{AC} = 0.1412\ \mu M/s$, A_c and S_p are the area of the cytosolic region and circumference of the plasma membrane of the annular cell geometry shown in Fig. 2b.

Thus,

$$\beta = \frac{E_{AC}A_c}{S_p} = \frac{E_{AC}\pi\left(R_o^2 - R_i^2\right)}{2\pi R_o} = 0.4503\ \mu M \cdot \mu m/s \tag{33}$$

Figure 5b shows the FEA vs analytical results for the time courses of cAMP signals at node 67 (on the plasma membrane), nodes 61 and 62 (within the cytosol) and node 75 (at the perinuclear region). The FEA results, once again, agreed very well with the analytical ones obtained from the solution developed for heat conduction in an annulus under flux boundary conditions and given in Sect. (b) in "Appendix 2".

4.2 Validation against other numerical solutions

In Sect. 4.1, no verification of the proposed FEA model was presented for cases where AC and PDE activities, together with the spatial spread of cAMP signals simultaneously contribute to cAMP signaling outcomes. The reason was that, to our best knowledge, no analytical solution, even for simple cellular geometry, is currently available for such verification.

To verify the implementation of all three components (cAMP synthesis, diffusion and degradation) of the proposed FEA model, we chose to rerun two simulations reported in [12] for the spherical cell geometry. For both simulations, AC activity was uniformly distributed along the plasma membrane and PDE activity was uniformly distributed throughout the cytosol. The only difference between the two simulations was the value of diffusion coefficient used ($D = 3\ \mu m^2/s$ and $0.3\ \mu m^2/s$). Note that the simulations in [12] were run using the finite volume solver available within the Virtual Cell environment [8] to solve a set of differential equations similar to (but not as general as) (Eq. 1).

Due to axisymmetry, the two problems involving the spherical cell geometry mentioned above can actually be solved using 2-D models. As a result, the FEA simulations herein were run on the annular cell geometry (a cross section of the spherical cell geometry) shown in Fig. 2b. As depicted in Fig. 6a, b, there is a very good agreement between our FEA results and the finite volume ones provided by Virtual Cell. Some noticeable discrepancy occurs along the plasma membrane (represented by
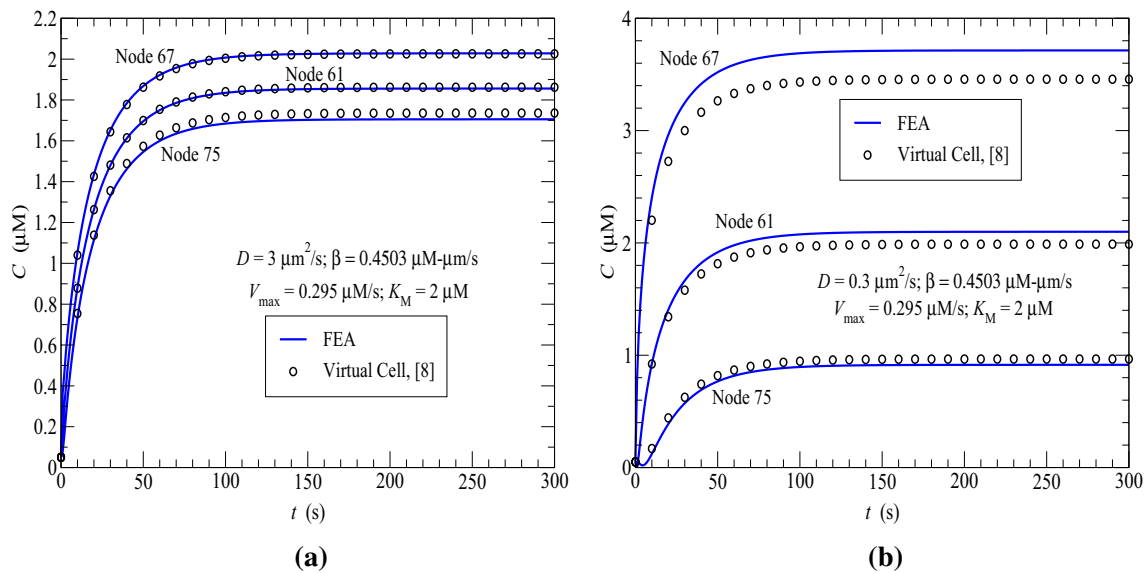
Fig. 6 FEA vs finite volume (Virtual Cell) solutions for the time course of cAMP concentration in response to AC activity (β = 0.4503 μM·μm/s) uniformly distributed along the plasma membrane and PDE activity uniformly distributed in the cytosol **a** D = 3 μm^2/s; **b** D = 0.3 μm^2/s

node 67, see Fig. 2b) for the case of D = 0.3 μm^2/s. However, no perfect agreement between the two solutions should be expected here as they were run on two different numerical methods (FVM vs FEM) and two different dimensions (3-D vs 2-D).

4.3 FEA simulations on the 2-D cultured PMVEC geometry

Finite element implementation of the governing Eq. (1) was successfully verified in Sects. 4.1 and 4.2. FEM is known as a powerful numerical technique for handling complex geometries governed by partial differential equations such as Eq. (1). Two FEA simulations in this section were run on the complex 2-D cultured PMVEC geometry shown in Fig. 2a. The objective herein is to demonstrate the potential performance of the proposed FEA model and its capability of simulating general situations of cAMP signaling that could be seen in experiments.

4.3.1 Uniform AC and PDE activities

In this simulation, AC activity was assumed to be uniformly generated on the plasma membrane via a positive flux β = 0.6826 μM·μm/s determined by Eq. (32) where A_c = 478.422 μm^2 and S_p = 51.066 μm are the area of the cytosolic region and circumference of the plasma membrane of the cultured PMVEC geometry. PDE

activity was uniformly taken place throughout the cytosol (V_{max} = 0.295 μM/s, K_M = 2 μM). Both AC and PDE activities started at $t_s = t_d = 0$, and D = 6 μm^2/s was employed for this simulation. A low diffusion coefficient was purposely chosen herein so the spatial spread of cAMP signals from the plasmalemmal to perinuclear regions can be clearly seen from an animation of the FEA results (see Fig. 7).

The FEA simulation was run using a final analysis time t_f = 300s and a time step Δt = 2.5s. Figure 7 shows the resulting spatial distribution of cAMP signals at six different time instants, namely, t = 5, 10, 15, 20, 40 and 100s. No additional figure of cAMP distribution beyond t = 100s is shown as the distribution almost reached its steady state 100s following the activation of AC and PDE. At time t = 5s (Fig. 7a), cAMP concentration can be seen to start increasing along the plasma membrane. Substantial cAMP gradients kept increasing up to around t = 40s (see Fig. 7b–e) when a large amount of cAMP signals could be seen moving toward the perinuclear region. At a later time (t > 100s, for example), as increasing cAMP concentrations led to stronger PDE reactions, a steady-state cAMP spatial distribution was quickly approached for this case. As expected and clearly shown in Fig. 7f, higher cAMP concentration can be seen in thinner regions of cytoplasm.

A combination of a color-filled contour map of the steady-state cAMP distribution (Fig. 8a) and a time-course plot of cAMP concentrations at three typical cellular locations (Fig. 8b) provides additional information about cAMP signaling for this simulation. It can be observed from Fig. 8a that, at the steady state of cAMP spatial distribution,
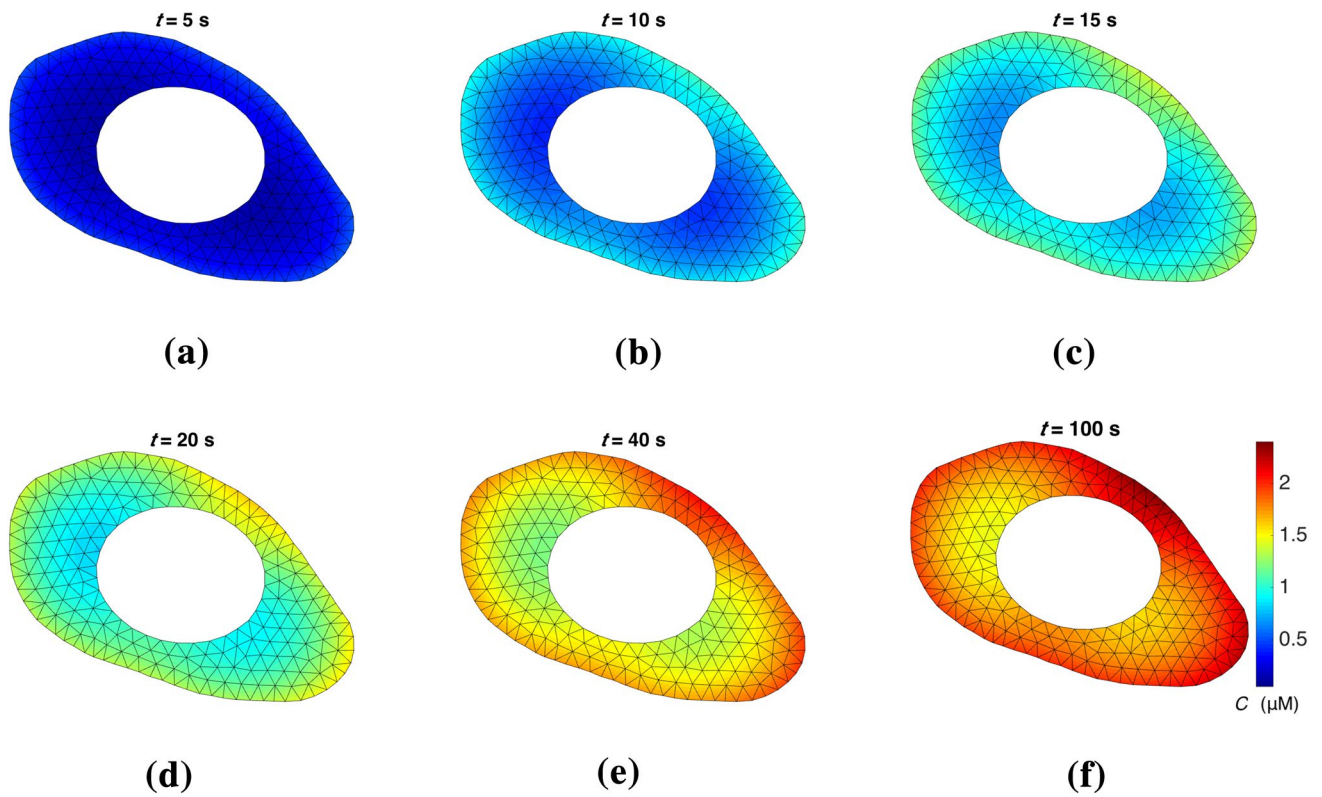
Fig. 7 Spatial distribution of cellular cAMP concentration at different time instants. AC activity was uniformly activated along the plasma membrane, PDE activity was uniformly distributed throughout the cytosol, and $D = 6\ \mu m^2/s$
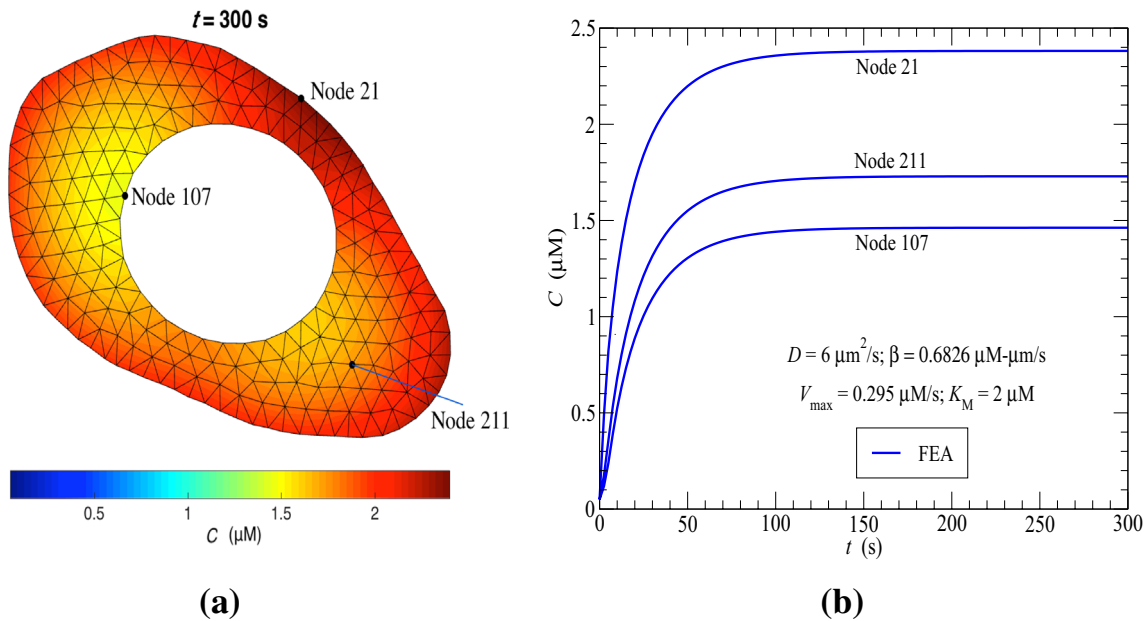

Fig. 8 FEA results with AC activity uniformly activated along the plasma membrane, PDE activity uniformly distributed in the cytosol and $D = 6\ \mu m^2/s$: **a** Distribution of cellular cAMP concentration at time $t = 300\ s$ (steady-state distribution); **b** Time course of cAMP concentration at nodes 21 (on the plasma membrane), 211 (in the cytosol) and 107 (at the perinuclear region)

the highest concentration occurred at the plasma membrane where cAMP synthesis was activated, the lowest concentration took place in the perinuclear region and a medium concentration occurred within the cytosol. For this simulation, the three locations mentioned above were represented by nodes 21, 107 and 211, respectively (see Fig. 8a). The time-course plots for the concentration at these three nodes were depicted in Fig. 8b where their steady states were reached after about 100s following the AC and PDE activation.

4.3.2 Localized AC and PDE activities

In the last simulation, in addition to uniform AC activity along the plasma membrane and uniform PDE activities throughout the cytosol, two localized AC sources were assumed to also take place on the plasma membrane and a localized PDE source was assumed to occur in the cytosol. Two localized AC sources were located within side 1–2 (a plasmalemmal segment bound by nodes 1 and 2) and side 39–40 (see Fig. 10a), and the localized PDE source was inside element 20 defined by nodes 212, 217 and 223. The total AC and PDE activities were kept the same as those given by Eqs. (29) and (30).

It was assumed that 55%, 20% and 25% of the total AC activity took place from time $t_d = 0$, 20s and 40s along the plasma membrane, on side 1–2 and on side 39–40, respectively. These three AC activities corresponded to three flux

values, namely $\beta = 0.3754, 9.7719, 13.6614$ μM·μm/s which were found by using Eq. (32) together with the area of the cytosolic region, the circumference of the plasma membrane and the lengths of sides 1–2 and 39–40 from the PMVEC geometry in Fig. 2a.

It was also assumed that 75% and 25% of the total PDE activity were uniformly distributed throughout the cytosol and enacted at a location within element 20 from time $t_d = 0$ and 30s, respectively. Using the areas of the cytosolic region and element 20, these two PDE activities resulted in two respective values of $V_{max} = 0.2213$ and 26.5790 μM/s.

The FEA simulation was run using the usual diffusion coefficient $D = 30$ μm^2/s, a final analysis time $t_f = 300$s and a time step $\Delta t = 1$s. A smaller time step needed to be employed here so the FEA can accurately capture several abrupt changes in the slope of the time-course plots due to the sudden activation of AC and PDE activities at different time instants.

Figure 9 shows six color-filled contour plots of the spatial distribution of cAMP signals at times $t = 10, 25, 35, 45, 60$ and 100s. No additional figure of cAMP distribution beyond $t = 100$s was needed as cAMP signals at this point almost reached their steady-state values. At time $t = 25$s (Fig. 9b), cAMP concentration can be seen to start increasing on side 1–2 where the first localized AC source was activated at $t_s = 20$s. At the same time, lower amount of cAMP signals were also shown around the
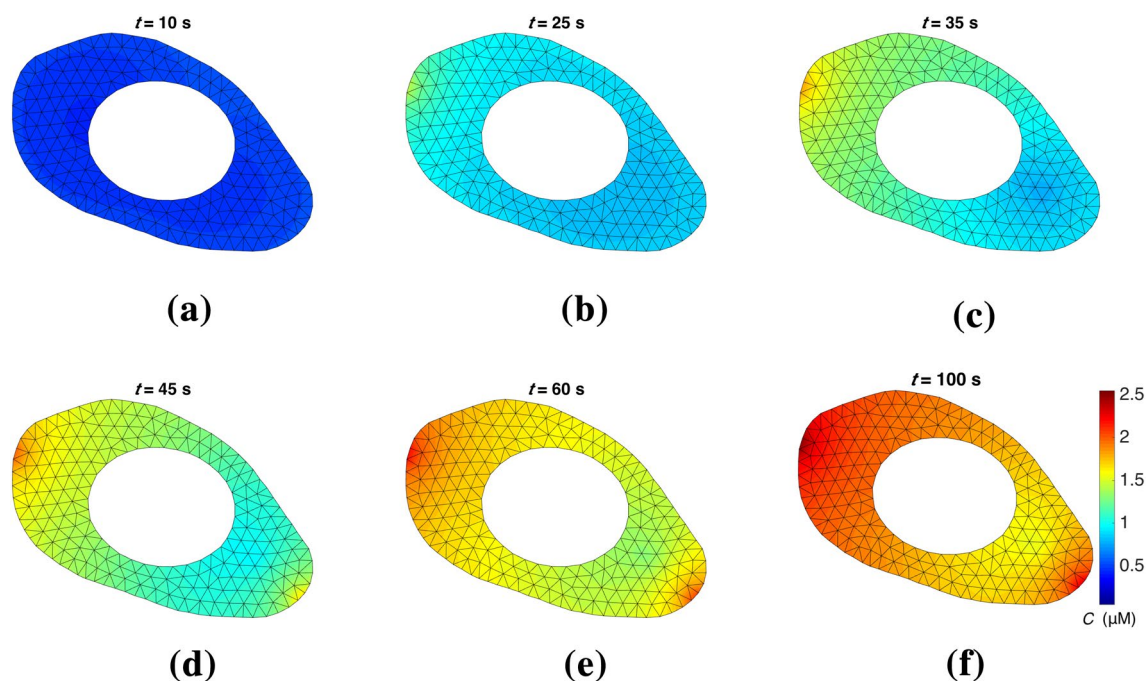

Fig. 9 Spatial distribution of cellular cAMP concentration at different time instants. AC activity was locally activated at the plasma membrane, PDE activity was locally activated in the cytosol
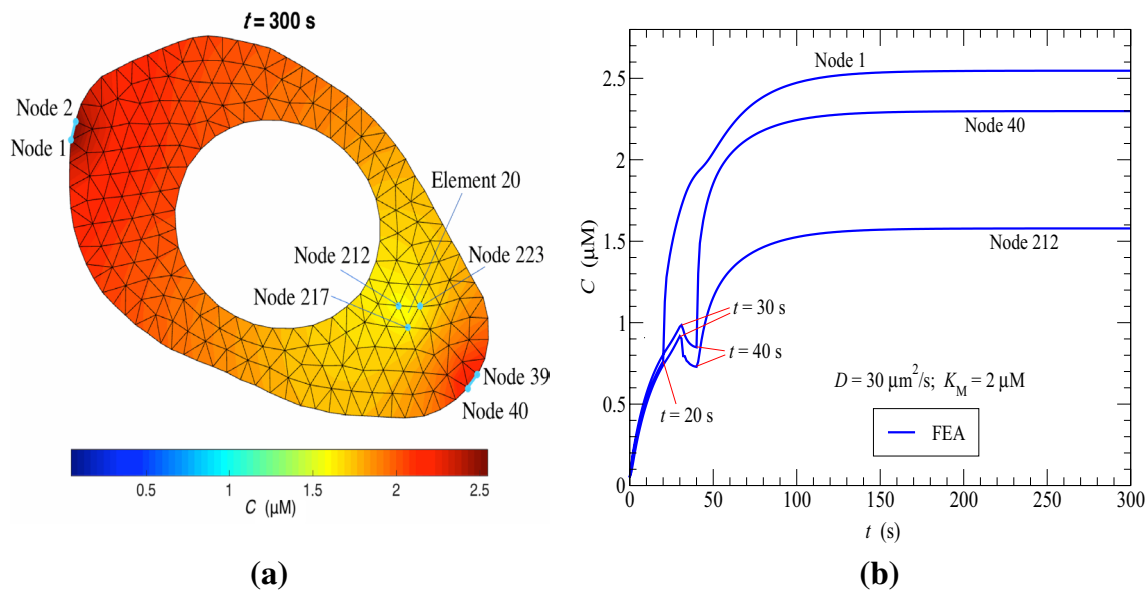
Fig. 10 FEA results with two localized AC activities on the plasma membrane, a localized PDE activity in the cytosol and $D = 30\ \mu m^2$ /s: **a** Distribution of cellular cAMP concentration at time $t = 300$ s (steady-state cAMP level); **b** Time course of cAMP concentration at nodes 1 (at the first localized AC source on the plasma membrane), 40 (at the second localized AC source on the plasma membrane) and 212 (at the localized PDE source in the cytosol)

plasma membrane due to the uniform AC activity in that region. At time $t = 35$s (Fig. 9c), a larger amount of cAMP signals was clearly seen around side 1–2 while the lowest amount of cAMP signals can be found at the location of element 20 where the localized PDE source was initiated at $t_d = 30$s. After the activation of the second localized AC source along side 39–40 at time $t_s = 40$s, Fig. 9d shows some increase of cAMP concentration in that area. The effect of two localized AC activities in the plasmalemmal region is clearly shown from the two red zones in Fig. 9e while the effect of the localized PDE activity in the cytosol can be seen from the green zone around element 20 in Fig. 9f.

Figure 10 depicts a side-by-side display of a color-filled contour plot of steady-state cellular cAMP signals and a time-course plot for cAMP signals at three distinct cellular locations: nodes 1, 40 and 212 at the locations of the first and second localized AC sources, and the localized PDE source, respectively.

As expected, there were some changes in the slope of the curves in Fig. 10b due to the effects of the localized AC and PDE activities that set off at different times. There was a quick increase in cAMP concentration at node 1 at time $t = 20$s (Node-1 curve) due to the start of the first localized AC activity on side 1–2. The triggering of the localized PDE activity in element 20 resulted in an abrupt drop in cAMP concentration at nodes 212 and the nearby node 40 at time $t = 30$s (see Node-40 and Node-212 curves). The activation of the second localized AC on side 39–40 caused

a sudden growth of cAMP signals at nodes 40 and nearby 212 at time $t = 40$s. Finally, although more percentage of the total AC activity occurred on side 39–40 (25%) than side 1–2 (20%), the presence of a nearby localized PDE source resulted in a lower value of the steady-state concentration at node 40 (2.30 μM) then at node 1 (2.55 μM).

5 Conclusion

In this work, a fundamental yet general 2-D FEA model for intracellular cAMP signaling was introduced. The model is able to simulate a variety of AC and PDE activities at different start time points. These activities can uniformly take place over the entire cytosol, plasma membrane or perinuclear region, or just over parts of these regions (localized activities), or a combination of these two forms. Numerical results produced by the model for a number of cAMP signaling cases including those under compartmental scenarios and those in a simple (annular) cell geometry were found to either excellently agree with available analytical solutions or agree very well with the numerical results obtained from the "Virtual Cell" environment. Overall, model simulations demonstrated that under certain conditions, sustained cAMP gradients can be formed within ECs, similar to those observed in rat PMVECs [25].

The proposed FEA model offers an effective tool for the study of second messenger signaling within the pulmonary vasculature. It is expected to compliment or

supplement experimental studies on intracellular cAMP signaling. While the data used to constrain this model were obtained from PMVECs, the model is applicable to a variety of cell types.

The results demonstrate that the finite element model is well suited to describe the spatial spread and kinetics of intracellular cAMP signals. The technique developed in Sect. 3 has the ability to expand the scale of this model from isolated cells to 2-D cellular arrays where the spatial spread of cAMP signals between cells via gap junctions can be simulated, and, eventually, to 3-D descriptions of cAMP signals within the pulmonary vasculature. Note that the steady-state enzyme kinetic Eq. (2) was derived under the assumption that the enzyme (PDE) concentration is well below the substrate (cAMP) concentration. Our previous work suggests that for many cellular systems this assumption is valid. For example, in PMVECs the concentration of PDE was experimentally estimated to be around 3 nM, which is substantially lower than free cAMP concentrations under baseline conditions [12]. However, there are notable exceptions in which PDE activity in a localized region of the cell may be higher than substrate concentration, including rod outer segments, olfactory cilia, and dendritic spines. For situations where the above assumption does not hold, the quadratic velocity (Morrison) equation [26] should be employed instead of the Michaelis–Menten kinetics. The validation of the proposed basic model is the first important step before this model can be expanded in a future work to include other PDE enzyme kinetics (such as the Morrison equation), to describe cAMP spread through organoid cultures of even tissues, and to describe a variety of G protein mediated signaling networks.

Compliance with ethical standards

Conflicts of interest Drs. Leavesley and Rich disclose financial interest in Spectracyte, LLC, a start-up company formed to commercialize spectral imaging technologies.

Appendix 1

The solution of the following initial value problem:

$$\frac{dC}{dt} = u - \frac{vC}{w + C} \; ; \quad C(0) = q \tag{34}$$

where u, v, w and q are constants, is given by

$$C(t) = \frac{w}{v - u}\left[u + vW\left(-\frac{1}{vw}\exp(U)\right)\right] \tag{35}$$

where $W()$ is the Lambert W function, and

$$U = \frac{1}{vw}\left[(u - v)^2\left(\frac{Bvw}{A} - t\right) - uw\right]$$
$$A = u^2 - v(2u - v) \tag{36}$$
$$B = \ln\left\{(uw + uq - vq)\exp\left[\frac{q}{w}\left(1 - \frac{u}{v}\right)\right]\right\}$$

If $u = 0$, the solution reduces to

$$C(t) = wW\left(\frac{q}{w}\exp\left[\frac{1}{w}(-vt + q)\right]\right) \tag{37}$$

If $v = 0$, the solution is simply given by

$$C(t) = ut + q \tag{38}$$

Appendix 2

The diffusion in a hollow cylinder is governed by the following partial differential equation:

$$\frac{\partial C}{\partial t} = \frac{D}{r}\frac{\partial}{\partial r}\left(r\frac{\partial C}{\partial r}\right); \quad a \le r \le b \tag{39}$$

where D is the diffusion coefficient, and a and b are the inner and outer radii of the cylinder.

(a) Concentration boundary conditions

$$C(a, t) = C_a \tag{40}$$

$$C(b, t) = C_b \tag{41}$$

$$C(r, 0) = C_o \; ; \quad a \le r \le b \tag{42}$$

The solution of Eq. (39) under these boundary and initial conditions is given by [24]

$$C(r, t) = \frac{C_a \ln(b/r) + C_b \ln(r/a)}{\ln(b/a) + \pi\left[C_o X(t) - Y(t)\right]} \tag{43}$$

where

$$X(t) = \sum_{n=1}^{\infty} \frac{V_n(t)}{J_o(a\alpha_n) + J_o(b\alpha_n)} \tag{44}$$

$$Y(t) = \sum_{n=1}^{\infty} \frac{\left[C_b J_o(a\alpha_n) - C_a J_o(b\alpha_n) \right] V_n(t)}{J_o^2(a\alpha_n) - J_o^2(b\alpha_n)} \tag{45}$$

$$V_n(t) = J_o(a\alpha_n) U_o(r\alpha_n) \exp(-D\alpha_n^2 t) \tag{46}$$

$$U_o(r\alpha_n) = J_o(r\alpha_n) Y_o(b\alpha_n) - J_o(b\alpha_n) Y_o(r\alpha_n) \tag{47}$$

In the above equations, α_n's are the positive roots of $U_o(a\alpha_n) = 0$, and J_o and Y_o are Bessel functions of the first and second kind of order zero, respectively.

(b) Flux boundary conditions

$$D\frac{\partial C(b,t)}{\partial r} = \beta \tag{48}$$

$$\frac{\partial C(a,t)}{\partial r} = 0 \tag{49}$$

$$C(r,0) = C_o ; \quad a \le r \le b \tag{50}$$

For these boundary and initial conditions, the solution of Eq. (39) can be found as [27],

$$C(r,t) = C_o + \frac{\beta b}{D} \left\{ \frac{2Dt + M(r)}{b^2 - a^2} \right.$$
$$\left. + \pi \sum_{n=1}^{\infty} \frac{J_1^2(\alpha_n a/b) N_n(r) \exp(-\alpha_n^2 Dt/b^2)}{\alpha_n \left[J_1^2(\alpha_n a/b) - J_1^2(\alpha_n) \right]} \right\} \tag{51}$$

where

$$M(r) = \frac{2r^2 - 3a^2 - b^2}{4}$$
$$+ \frac{a^2}{b^2 - a^2} \left[a^2 \ln\left(\frac{r}{a}\right) - b^2 \ln\left(\frac{r}{b}\right) \right] \tag{52}$$

$$N_n(r) = J_o(\alpha_n r/b) Y_1(\alpha_n) - J_1(\alpha_n) Y_o(\alpha_n r/b) \tag{53}$$

In these equations, J_1 and Y_1 are Bessel functions of the first and second kind of order one, respectively, and α_n's are the positive roots of

$$J_1(\alpha_n a/b) Y_1(\alpha_n) - J_1(\alpha_n) Y_1(\alpha_n a/b) = 0 \tag{54}$$

References

1. Mehats C, Andersen CB, Filopanti M, Jin SL, Conti M (2002) Cyclic nucleotide phosphodiesterases and their role in endocrine cell signaling. Trends Endocrinol Metab 13:29–35
2. Conti M, Beavo J (2007) Biochemistry and physiology of cyclic nucleotide phosphodiesterases: essential components in cyclic nucleotide signaling. Annu Rev Biochem 76:481–511
3. Penn RB (2008) Embracing emerging paradigms of G protein-coupled receptor agonism and signaling to address airway smooth muscle pathobiology in asthma. Naunyn Schmiedebergs Arch Pharmacol 378:149–169
4. Bobin P, Belacel-Ouari M, Bedioune I, Zhang L, Leroy J, Leblais V, Fischmeister R, Vandecasteele G (2016) Cyclic nucleotide phosphodiesterases in heart and vessels: a therapeutic perspective. Arch Cardiovasc Dis 109:431–443
5. Rich TC, Karpen JW (2002) Cyclic AMP sensors in living cells: what signals can they actually measure? Ann Biomed Eng 30:1088–1099
6. Rich TC, Webb KJ, Leavesley SJ (2014) Perspectives on: cyclic nucleotide microdomains and signaling specificity: can we decipher the information content contained within cyclic nucleotide signals? J Gen Physiol 143:17–27 PMCID: PMC3874573
7. Conti M, Mika D, Richter W (2014) Cyclic AMP compartments and signaling specificity: role of cyclic nucleotide phosphodiesterases. J Gen Physiol 143:29–38 PMCID: PMC3874571
8. Schaff J, Fink CC, Slepchenko B, Carson JH, Loew LM (1997) A general computational framework for modeling cellular structure and function. Biophys J 73:1135–1146
9. Williamson T, Schwartz J-M, Kell DB, Lubomira S (2009) Deterministic mathematical models of the cAMP pathway in *Saccharomyces cerevisiae*. BMC Syst Biol 3:70
10. Oliveira RF, Terrin A, Di Benedetto G, Cannon RC, Koh W, Kim M, Zaccolo M, Blackwell KT (2010) The role of type 4 phosphodiesterases in generating microdomains of cAMP: large scale stochastic simulations. PLoS ONE 5(7):e11725
11. Rich TC, Xin W, Mehats C, Hassell KA, Piggott LA, Le X, Karpen JW, Conti M (2007) Cellular mechanisms underlying prostaglandin-induced transient cAMP signals near the plasma membrane of HEK-293 cells. Am J Physiol Cell Physiol 292(1):C319–C331
12. Feinstein WP, Zhu B, Leavesley SJ, Sayner SL, Rich TC (2012) Assessment of cellular mechanisms contributing to cAMP compartmentalization in pulmonary microvascular endothelial cells. Am J Physiol Cell Physiol 302(6):C839–C852
13. Saucerman JJ, Greenwald EC, Polanowska-Grabowska R (2014) Mechanisms of cyclic AMP compartmentation revealed by computational models. J Gen Physiol 143(1):39–48
14. Rich TC, Fagan KA, Nakata H, Schaack J, Cooper DM, Karpen JW (2000) Cyclic nucleotide-gated channels colocalize with adenylyl cyclase in regions of restricted cAMP diffusion. J Gen Physiol 116:147–161
15. Karpen JW, Rich TC (2001) The fourth dimension in cellular signaling. Science 293:2204–2205
16. Agarwal SR, Miyashiro K, Latt H, Ostrom RS, Harvey RD (2017) Compartmentalized cAMP responses to prostaglandin EP2 receptor ctivation in human airway smooth muscle cells. Br J Pharmacol 174:2784–2796
17. Salter RC, Webb KJ, Phan A-V, Rich TC (2014) A finite element model of the synthesis, degradation, and spatial spread of cAMP. In: Proceedings of the 14th annual early career technical conference, Birmingham
18. Shettlesworth S, Webb KJ, Phan A-V, Rich TC (2016) A 3-D finite element model of the synthesis, degradation, and spatial spread of cAMP. In: 2016 ASME early career technical conference, Birmingham

19. Stryer L (1995) Biochemistry. W.H. Freeman and Company, New York

20. Rich TC, Fagan KA, Tse TE, Schaack J, Cooper DMF, Karpen JW (2001) A uniform extracellular stimulus triggers distinct cAMP signals in different compartments of a simple cell. Proc Natl Acad Sci 98(23):13049–13054

21. Bhatti MA (2005) Fundamental finite element analysis and applications: with mathematica and matlab computations. Wiley, Hoboken

22. Bathe KJ (1996) Finite element procedures. Prentice-Hall, Englewood Cliffs

23. Persson PO, Strang G (2004) A simple mesh generator in MATLAB. SIAM Rev 46(2):329–345

24. Carslaw HS, Jaeger JC (1959) Conduction of heat in solids. Clarendon Press, Oxford

25. Annamdevula NS, Sweat R, Griswold JR, Trinh K, Hoffman C, West S, Deal J, Britain AL, Jalink K, Rich TC, Leavesley SJ (2018) Spectral imaging of FRET-based sensors reveals sustained cAMP gradients in three spatial dimensions. Cytometry A 93(10):1029–1038

26. Morrison JF (1969) Kinetics of the reversible inhibition of enzyme-catalysed reactions by tight-binding inhibitors. Biochim Biophys Acta Enzymol 185(2):269–286

27. Cole KD, Beck JV, Haji-Sheikh A, Litkouhi B (2011) Heat conduction using Green's functions, 2nd edn. CRC Press, Boca Raton